Renée M. Ripken[1,2]
Jeffery A. Wood[3]
Johannes G. E. Gardeniers[2]
Séverine Le Gac[1,*]

Aqueous-Phase Reforming in a Microreactor: The Role of Surface Bubbles

In heterogeneous catalysis, the creation of gaseous products as bubbles in a liquid phase on the catalytic surface is associated with slip phenomena. In a microreactor, the slip length at the gas-liquid interface is in the same order of magnitude as the reactor dimensions, which can affect fluid dynamics and transport phenomena. Here, the interplay of momentum, heat and mass transfer in a microreactor, when bubbles form on the catalytic surface, was investigated using two-dimensional simulations. The effect of bubbles on the endothermic process of aqueous-phase reforming of a glycerol solution was evaluated in terms of conversion and conversion and temperature in the reactor. Altogether, this study highlights the impact of bubbles, not only on the transport phenomena but also on the reactor performance.

Keywords: Bubbles, Heat and mass transport, Heterogeneous catalysis, Microfluidics, Slip velocity

Received: February 27, 2019; *revised:* April 11, 2019; *accepted:* July 04, 2019

DOI: 10.1002/ceat.201900142

Supporting Information available online

1 Introduction

Many industrial chemical processes comprise one or multiple catalytic reactions. For large-scale production, heterogeneous catalysis is preferred, in which a solid-phase catalyst is used while reactants, products, and solvent are in the gaseous and/or liquid phase. In some catalytic reactions, such as aqueous-phase reforming (APR) [1], gaseous products (CO, CO_2, H_2) form as bubbles on the catalytic surface in the liquid reaction mixture, resulting in a three-phase system. The interplay of the different transport phenomena in such multiphase systems is relatively complex due to the differences in the physical properties of the fluids and the competing effects in transport phenomena, which altogether impact the resulting chemical conversion and reactor performance.

Microfluidics is an ideal platform to study heat and mass transfer in such multiphase systems [2–5]. These miniaturized systems not only offer accurate fluid control, but also exhibit excellent heat and mass transfer properties as a result of their large surface-to-volume ratio [6–8]. In microfluidic systems, the solid catalyst can be introduced as a packed bed [9, 10], a monolithic phase (foam) [11, 12], or a thin-layer on the microchannel walls [13, 14]. Furthermore, and particularly, reactions suffering from slow kinetics benefit from the large catalytic surface area offered by microreactors.

However, the presence of bubbles on the catalytic surface is highly undesirable, particularly in a microreactor, as they block the catalytic surface, thereby preventing further reaction, obstructing liquid flow, and also possibly negatively impacting the temperature profile. At the same time, bubbles give no-shear interfaces, so that they can promote mixing and/or reduce drag forces (if no surfactant is added to the system) by providing effective slip [15, 16]. Typically, slip is quantified by the slip length b[1)], expressed as:

$$b = \delta\left(\frac{\mu_l}{\mu_g} - 1\right) \cong \delta\frac{\mu_l}{\mu_g} \tag{1}$$

where δ is the thickness of the gas layer, and μ_i denotes the viscosity of the liquid (l) or gas (g) [17]. Due to the large viscosity difference between gases and liquids, the slip length for bubbles can be in the order of micrometers. As microreactors have dimensions in the same micrometer range, such a slippery interface near or on a catalytic surface cannot be neglected [18].

As a result of the slip velocity, convection is locally increased, which is also influencing transport phenomena [19]. In

1) List of symbols at the end of the paper.

[1]Dr. Renée M. Ripken, Prof. Dr. Ir. Séverine Le Gac
s.legac@utwente.nl
University of Twente, Applied Microfluidics for BioEngineering Research, MESA+ Institute for Nanotechnology, TechMed Centre, P.O. Box 217, 7500 AE Enschede, The Netherlands.
[2]Dr. Renée M. Ripken, Prof. Dr. Johannes G. E. Gardeniers
University of Twente, Mesoscale Chemical Systems, MESA+ Institute for Nanotechnology, P.O. Box 217, 7500 AE Enschede, The Netherlands.
[3]Dr. Jeffery A. Wood
University of Twente, Soft Matter, Fluidics and Interfaces, MESA+ Institute for Nanotechnology, P.O. Box 217, 7500 AE Enschede, The Netherlands.

previous work, Karatay et al. studied the dissolution of protruding gas bubbles in liquid in a microreactor operating under laminar flow conditions [20]. In that work, an array of elliptical or hemispherical bubbles was considered, forming a bubble mattress, which shares similarities with the case where bubbles are formed as products of a reaction such as APR. Interestingly in that work [20], depending on the exact bubble geometry, mass transport was enhanced in the channel due to the slippage at the gas-liquid interface.

Here, we investigated the effect of a bubble mattress on the momentum, heat and mass transport to and from a catalytic surface, using COMSOL Multiphysics 5.3a [21] and a 2D numerical simulation. Specifically, APR of glycerol was considered as a model reaction. APR is an endothermic reaction, so that bubbles can play an important role in terms of thermal transfer, potential slip, and loss of catalytic surface area. The transport phenomena (momentum, thermal and mass) and the resulting reactor conversion were evaluated as a function of the bubble characteristics, i.e., length, protrusion angle, and catalytic surface coverage, at two temperatures to explore the possible impact of bubbles on the microreactor performance.

2 Experimental

2.1 2D Microreactor Geometry

A 2D model was considered to evaluate the momentum, heat and mass transfer in a catalytic microreactor, in which bubbles grew on a solid catalytic surface (Fig. 1). This 2D geometry was derived from a previously described silicon/glass microfluidic device [22]. Briefly, a 250-µm deep fluidic channel was created in a silicon substrate and covered by a glass top layer. This microchannel was considered as infinitely wide. A 10-µm thick TiO_2 layer on the silicon acted as a model catalyst. The catalytic reaction occurred at this boundary, where only external mass transport was taken into account. The device was heated from the silicon side using an external MgO ceramic heater. Heat was allowed to dissipate either through the glass cover or via the inlet and outlet; the remainder of the geometry was considered thermally insulated.

A bubble mattress with hemispherical/elliptical H_2 bubbles, depending on the protrusion angle, was modeled on the TiO_2 surface as products of the catalytic reaction. These bubbles were described by their characteristic length (L_g), their protrusion angle into the liquid (α), and the fraction of the catalytic surface covered by the bubbles (ε_B), and all these parameters were varied in the simulations (see Tab. 1). A slip boundary condition was imposed on the bubble-liquid interface, and a no-slip boundary condition on the channel walls. The bubbles were treated as non-deformable and set at a fixed position in the microchannel.

Table 1. Parametric sweep values: the bubble characteristics and heater temperature were varied to study their influence on the momentum, heat and mass transfer.

Parameter	Values
Protrusion angle α [°]	10; 45; 90
Characteristic gas bubble length L_g [µm]	20; 100
Fraction of the catalytic surface covered by bubbles ε_B	0.25; 0.5; 0.75
Heater temperature T_H [K]	525; 725

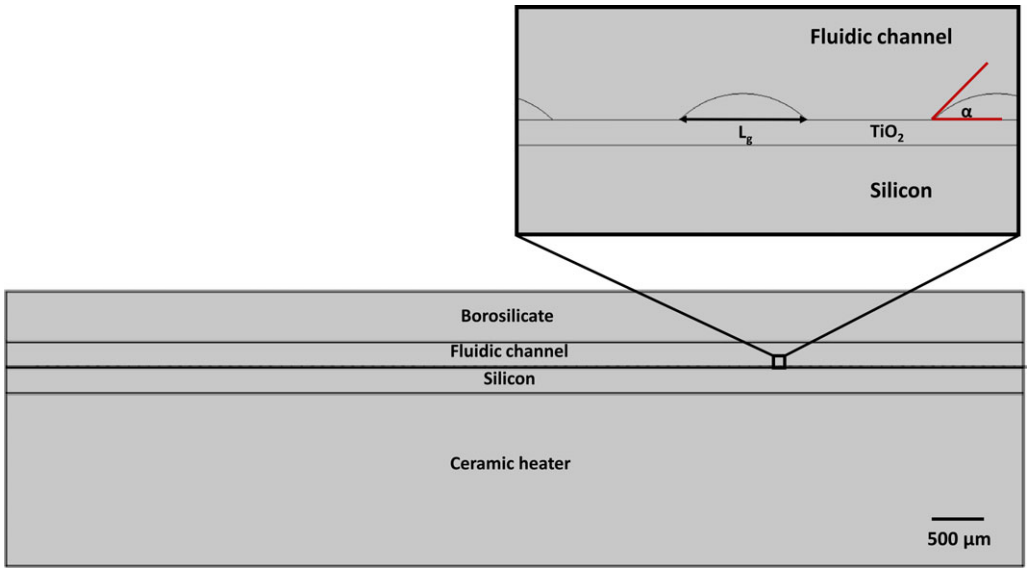

Figure 1. Schematic representation of the 2D microreactor geometry considered for the COMSOL simulations; the different materials for each layer are indicated. The temperature is regulated from the silicon side using an external ceramic heater. The characteristic bubble length and protrusion angle are denoted with L_g and α, respectively.

2.2 Catalytic Model Reaction

APR was considered as a model reaction. In APR, oxygenated carbohydrates, such as alcohols and sugars, with a 1:1 C:O ratio, herein referred to as biomass substrates, are reformed into CO_2 and H_2 in two main steps [1, 23]. First, the biomass substrate is cracked into CO and H_2, of which CO then reacts in the water-gas shift reaction to form CO_2 and additional H_2. Per definition, both reactions take place in the liquid phase on the same catalytic surface, which commonly consists of a noble metal on an oxide [23]. Typically, APR is performed at around 525 K,, as the reaction is endothermic, so that a 30-bar pressure must be applied to keep the reaction mixture in the liquid phase [23]. Here, a 10 wt % glycerol aqueous solution was considered as the biomass model substrate, and APR was modeled with first-order reaction kinetics (see Supporting Information S2).

2.3 Governing Equations

The fluid dynamics was evaluated by solving the steady-state Navier-Stokes equation for compressible fluids (Eq. (2)), and the continuity equation (Eq. (3)).

$$\rho(\vec{u}\cdot\nabla)\vec{u} = -\nabla P + \nabla\cdot\mu\left[(\nabla\vec{u}) + (\nabla\vec{u})^T\right] + \overrightarrow{f_g} \tag{2}$$

$$\nabla\cdot(\rho\vec{u}) = 0 \tag{3}$$

with ρ being the density and μ the viscosity of the liquid phase, $\overrightarrow{u}$ the average mean velocity, P the pressure, and $\overrightarrow{f_g}$ the volume force due to gravity (buoyancy).

The heat transfer, as described by Eqs. (4) and (5), was scaled to the inlet and heater temperatures, which were, respectively, 293.15 K and 525 K or 725 K.

$$\rho C_p\vec{u}\cdot\nabla T + \nabla\cdot\vec{q} = 0 \tag{4}$$

with:

$$\vec{q} = -k\nabla T \tag{5}$$

where C_p is the heat capacity, T the temperature, q the heat flux, and k the thermal conductivity.

The concentration profile in the bulk of the microchannel was computed by solving the convection-diffusion equation, while neglecting thermodiffusion effects:

$$\nabla\cdot\left(-D_{Gly}\nabla c_{Gly} + \vec{u}c_{Gly}\right) = 0 \tag{6}$$

where D_{Gly} and c_{Gly} indicate the diffusivity constant and concentration of glycerol. During the simulations, the bubble length, protrusion angle, and the catalytic surface coverage were varied to study their influence on the momentum and the heat and mass transfer, as summarized in Tab. 1, and two temperature values (525 K, 725 K) were considered. Temperature-dependent physical properties were included, as those can have a large impact in the system. Supporting Information S1 provides a list of the expressions and corresponding references.

At low protrusion angles (below 45°) positive slip lengths were expected, and negative slip at higher angles [20]. The low temperature value (525 K) corresponded to a typical APR reaction temperature [1], whereas the upper temperature limit (725 K) refers to the maximum temperature, at which our microreactor can operate [22].

Dimensionless variables:

The system geometry was scaled to the channel height, as well as other domain variables, for the purpose of numerical stability and to understand the relative contribution of various transport mechanisms. The dimensionless forms of the domain variables are as follows:

$$\bar{u} = \frac{\vec{u}}{u_0} \quad \bar{T} = \frac{T - T_0}{T_H - T_0} \quad \bar{c} = \frac{c_{Gly}}{c_0} \tag{7}$$

The dimensionless value of pressure is arbitrary since all liquid properties are pressure-independent. T_0 was 293.15 K, u_0 1.25 mm s^{-1}, and c_0 1.09 mol L^{-1}. T_H denotes the heater temperature.

2.4 Boundary Conditions

2.4.1 Momentum Transport (Velocity/Pressure)

The dimensionless inlet fluid velocity was set at a constant value of 1, so that the inlet velocity profile was fully developed before entering the fluidic channel at the inlet with an average velocity of u_0. The bubble-liquid interface was treated as no-shear since there were no surfactants or other effects expected to reduce the interface to no-slip [17, 20], which was considered as the best-case scenario for a microsystem with bubbles. The top wall of the microchannel and the catalytic surface were treated as no-slip and the outlet was set as a constant pressure outflow condition.

2.4.2 Energy Transport (Temperature)

The bottom of the ceramic heater was fixed at a specific temperature, assuming that the maximum power output of the heater was sufficient to maintain this temperature despite any loss to the environment or from the endothermic reaction. The inlet fluid temperature was set at 293.15 K, and the heat of reaction was taken into account at the interface of the fluid and the catalytic surface. The top of the glass layer was set at a constant ambient temperature of 293.15 K and treated as a heat flux using a heat transfer coefficient of 10 W $m^{-2}K^{-1}$, which is a typical value for natural convection [24, 25]. Continuity of temperature was assumed for all other internal boundaries.

2.4.3 Mass Transport (Concentration)

The concentration of glycerol in the microchannel was fixed at an arbitrary constant concentration (dimensionless value of 1) at the channel inlet, and assumed to be sufficiently low for applying Fick's law. At the catalyst surface, a first-order

reaction rate model was employed with a temperature-dependent rate constant introduced via an Arrhenius expression (Supporting Information S2) [26]. A dimensionless rate constant (Damköhler number) was calculated based on the characteristic dimensions of the reactor and rate constant at the reference temperature. For the bubble-liquid interface and top wall of the microchannel a no-flux boundary condition was prescribed. The outlet of the system was treated as a Neumann condition (zero normal gradient in concentration).

2.4.4 Simulation Details

The aforementioned equations were solved numerically for steady-state profiles using the finite element method in COMSOL Multiphysics 5.3a™ [21]. For the temperature and the concentration, second-order Lagrange polynomials were used and for the velocity/pressure a P2-P1 basis was selected. Mesh independency was confirmed based on successive refinement and resolution for the smallest bubble size and coverage considered.

3 Results and Discussion

3.1 Velocity, Temperature, and Concentration Profiles

First, the velocity and temperature profiles as well as the conversion were studied in a bubble-free microfluidic channel. The velocity profile was found to be consistent with a laminar flow profile and a no-slip boundary condition at the microchannel wall. Fig. 2 depicts the temperature (a) and glycerol concentration profiles (b) in the considered 2D microreactor for the endothermic APR reaction of glycerol at 525 K. Further downstream (increasing $x\,L^{-1}$), the glycerol concentration decreased in the channel, as a result of the APR reaction. As the reaction is endothermic, the temperature in the channel declined in the flow direction. The average dimensionless temperature at the outlet of the device was 0.84, which corresponds to a physical temperature of 488 K, whereas the average outlet conversion reached 0.56.

The same analysis was performed with a bubble mattress (L_g = 20 µm; α = 45°, ε_B = 0.5) at the same heater temperature. Fig. 3 depicts the velocity, concentration, and temperature profiles around the first three bubbles at the inlet of the fluidic channel. The average conversion determined at the outlet of the microreactor in the presence of bubbles was 0.46, which is lower than in the absence of bubbles.

From a global perspective, the velocity, temperature, and concentration profiles seemed to be very similar to the bubble-free case. However, when considering the liquid-bubble interface, the velocity contour lines were much closer at the top of the bubbles than near the channel wall, which indicates a steeper velocity gradient at the gas-liquid interface, due to the no-shear surface of the bubbles (Fig. 3 a). The concentration profile (Fig. 3 b) was directly related to the position of the bubbles since no reaction could occur either on the bubble or on the catalytic surface covered by bubbles.

The temperature profile (Fig. 3 c) was found to be almost uniform across the channel height, with only a small temperature gradient near the bubble-liquid interface. The lateral temperature gradient was very small, which can be explained by the relatively high thermal conductivity of hydrogen compared to other gases, which are more insulating [27]. The slightly higher temperature in the bubble than in the fluid may be counter-intuitive. However, since APR is an endothermic reaction, heat is only extracted at the catalytic surface area not covered by bubbles. Therefore, the temperature was lower at the catalytic surface than in the bubbles. Furthermore, the presence of a slip velocity at the bubble-liquid interface could not compensate for the temperature gradient resulting from the reaction. Altogether, while the endothermic character of the reaction dictates the temperature profile in the microchannel, adequate heat transfer through the insulating TiO_2 catalytic layer is essential for proper functioning of the microreactor and providing energy to conduct the APR conversion.

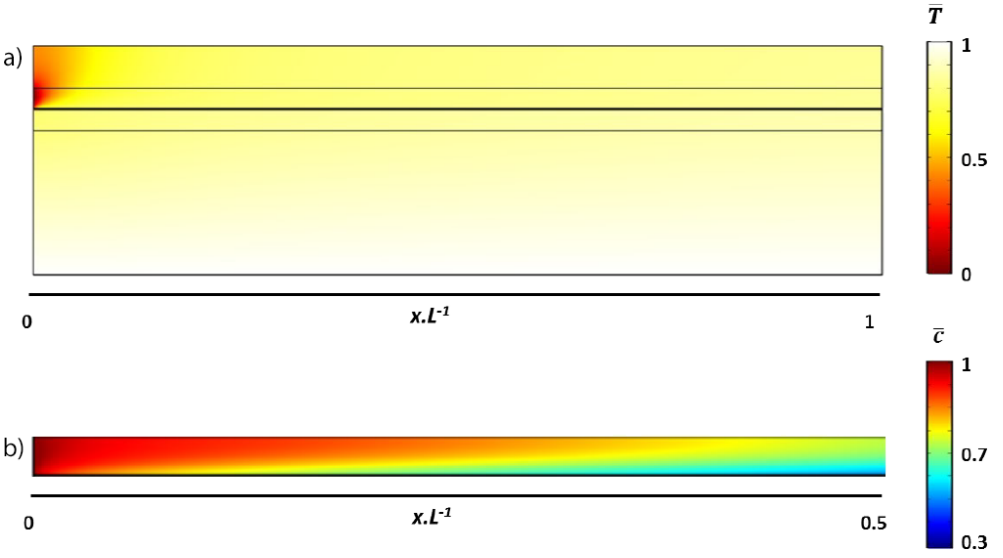

Figure 2. Dimensionless temperature profile over the entire microfluidic device (a) and dimensionless glycerol concentration profile from the inlet to halfway in the fluidic channel (b) in the absence of bubbles and at a heater temperature of 525 K.

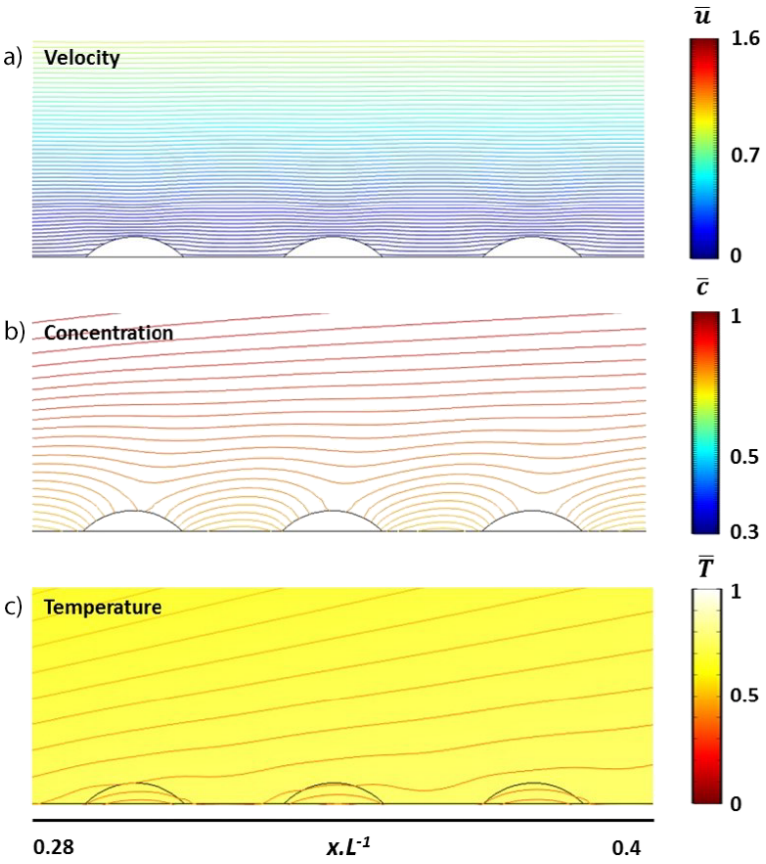

Figure 3. Dimensionless velocity (a), glycerol concentration (b), and temperature profiles (c) at the inlet of the microfluidic channel around the first three bubbles (L_g = 20 µm; α = 45°, ε_B = 0.5) when a temperature of 525 K was applied.

3.2 Effect of the Bubble Mattress Parameters on the Conversion

To study how the presence of bubbles could affect the chemical conversion, a parametric sweep was run by varying the bubble length, protrusion angle, and catalytic surface coverage. The conversion was evaluated at four positions in the fluidic channel. As illustrated in Fig. 4, bubbles negatively influenced the conversion, both at 525 K and 725 K, and the higher the temperature, the higher the glycerol conversion, as predicted by the Arrhenius equation.

The effect of the bubble mattress characteristics on the conversion was investigated in more detail. The conversion was normalized to the available catalytic surface area ($1-\varepsilon_B$) and plotted as a function of the same parameter, to determine how effectively the catalytic surface was used.

Fig. 5 compares two specific scenarios, with bubbles of 20 µm in length and a protrusion angle of 10° (square symbols), and bubbles of 100 µm in length and a protrusion angle of 90° (circle symbols). In general, the bubble characteristics (length and protrusion angle) were found to only influence the conversion rate at a high catalytic surface coverage by the bubbles (high ε_B). For $1-\varepsilon_B$ = 0.25, the highest conversion rate was achieved for shorter and flatter bubbles (L_g = 20 µm; α = 10°) for both considered temperatures. For such bubbles, a higher degree of slip is expected, so that they are less detrimental for the conversion than larger bubbles.

As demonstrated in both Figs. 5 a and 5 b, the conversion per available unit of catalytic surface area dropped when increasing the available catalytic surface area, which is likely due to a temperature effect: when a larger catalytic surface area was available to the liquid, more heat was utilized for the reaction, which in turn resulted in a lower temperature in the channel and led to a lower conversion.

3.3 Temperature

Finally, the temperature profile was evaluated in the microchannel for different bubble characteristics and applied temperatures. Fig. 6 depicts the temperature as a function of the *x*-position in the channel, for both heater temperatures, measured at the half-height of the fluidic channel. For sake of clarity, only non-overlapping data are depicted in Fig. 6. Surprisingly, the temperature was higher in the presence of bubbles, for all considered bubble

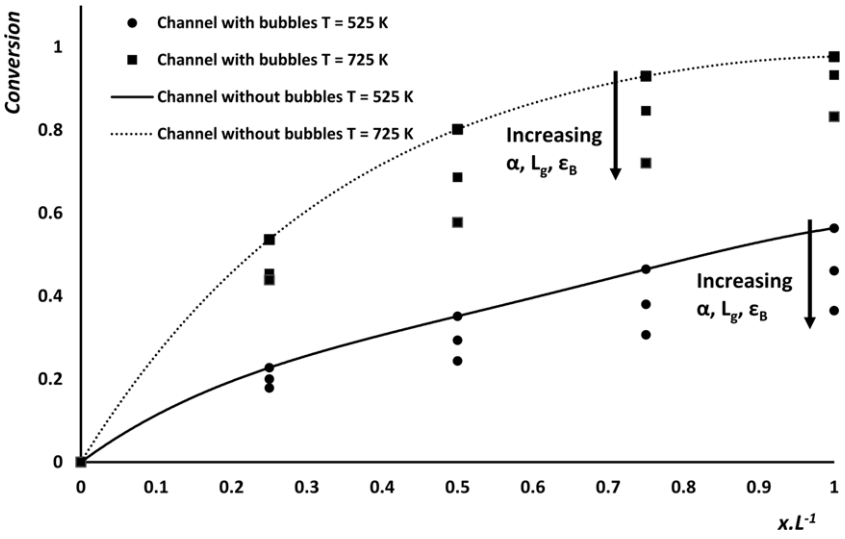

Figure 4. Chemical conversion as a function of the position in the fluidic channel for different bubble mattress characteristics. Squares (■) and triangles (●) indicate heater temperatures of 725 K and 525 K, respectively. The curves depict the conversion in the absence of bubbles.

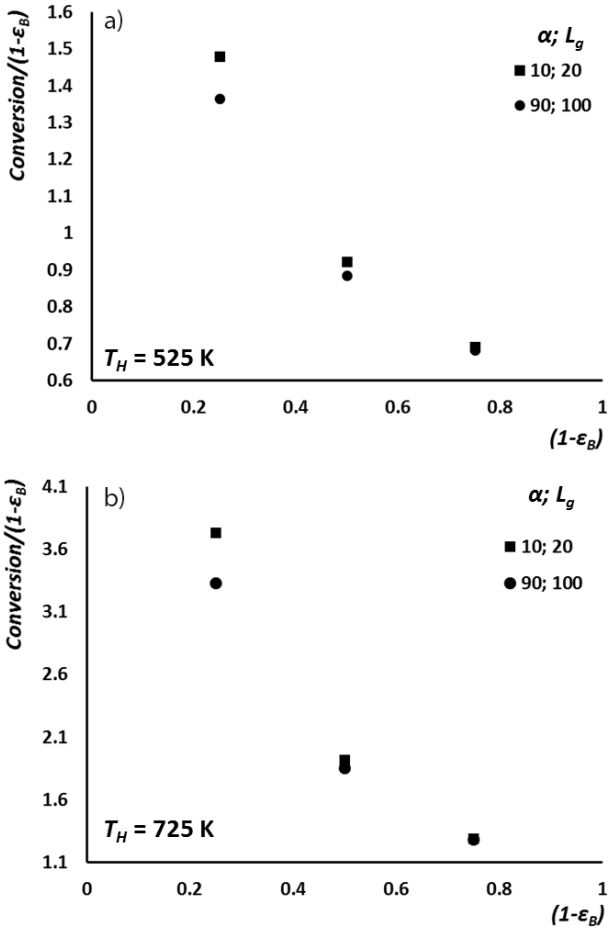

Figure 5. Conversion normalized to the available catalytic surface (1–ε_B) as a function of the available catalytic surface (1–ε_B), for a heater temperature of 525 K (a) and 725 K (b). (■) Bubbles of 20 μm in length with a protrusion angle of 10°, (●) bubbles of 100 μm in length and a protrusion angle of 90°.

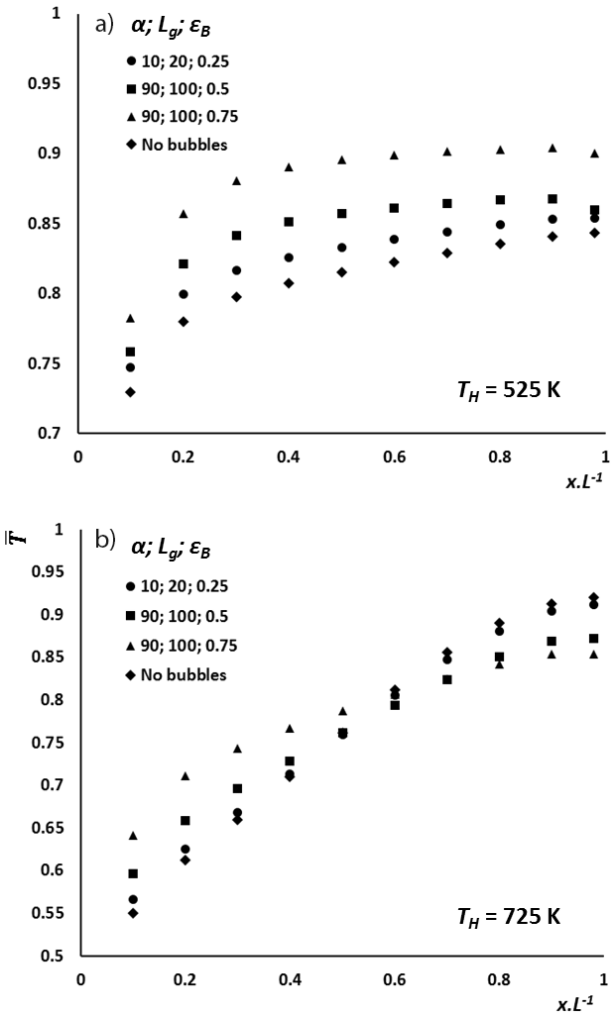

Figure 6. Dimensionless temperature profile at the half height of the fluidic channel as a function of the position in the channel for various bubble mattress characteristics and a heater temperature of 525 K (a) and 725 K (b).

configurations compared to a bubble-free situation. The highest temperature was obtained for bubbles characterized by $\alpha = 90°$ and $L_g = 100$ μm, and a catalytic surface coverage ε_B of 0.75.

These results are counter-intuitive since a higher catalytic surface coverage ε_B would be expected to correspond to a larger insulating layer, which should therefore prevent heat transfer. However, the temperature profile as depicted in Fig. 6 supports the trends observed for the reaction conversion (Fig. 4). For a lower conversion rate, less heat was used for the reaction, which overall resulted in a higher temperature in the channel. Altogether, the temperature in the fluid was mainly dictated by the chemical conversion, for which the heat transfer through the catalytic layer was limiting. Furthermore, in this work, hydrogen bubbles were considered, which have a relatively high thermal conductivity compared to other gases [27]. Thus, the effect of H_2 bubbles on the heat transfer was relatively smaller than for more insulating gases.

Next, three different temperature regions could be distinguished, which were mainly determined by the available catalytic surface coverage (1–ε_B) since the bubble protrusion angle and length did not significantly affect the temperature at the half height of the fluidic channel. At an applied temperature of 525 K, the relation between the temperature and the bubble mattress characteristics (L_g, α, ε_B) was straightforward: the temperature in the channel increased with the catalytic surface coverage ε_B.

A similar trend was observed for $x\,L^{-1}$ smaller than 0.6, and an applied temperature of 725 K. Further downstream in the channel, this situation was reversed, and higher temperatures were found in bubble-free channels. In the absence of bubbles, full chemical conversion was achieved at this specific location in the channel, so that no more heat was used for the endothermic APR reaction and all energy was transferred to the fluid. As full conversion was achieved at a later location in the presence of bubbles, heat was still used for the chemical reaction, so that the temperature remained lower in the channel than in the bubble-free configuration.

Overall, heat and mass transfer were found to depend on the degree of conversion, which was in turn determined by the catalytic surface coverage ε_B. As the herein considered reaction is endothermic, the conversion and, more indirectly, the catalytic surface coverage dominated the temperature profile. Overall, the slip velocity on the no-shear bubble-liquid interface was found to not play a significant role in the transport phenomena. In systems where gas bubbles inevitably form on the catalytic surface, applying a higher heater temperature can aid to counteract the negative effects of bubbles. At higher temperature, diffusion would also be enhanced, which would promote mass transfer towards and from the catalytic surface.

3.4 Model Relevance

Several aspects must be considered when translating the results of this study to an actual catalytic microreactor. First of all, in this work, a 2D model was used, with channels having an infinite width, while in an experimental microreactor the fluid is also confined by side walls. As the microchannel width is comparable to its depth, gradients caused by the presence of the side walls cannot be neglected.

The model could also be extended to include the bubble nucleation and growth. Product gases are expected to dissolve into the liquid until their maximum solubility is reached, as described by Henry's law. Once the liquid is saturated, bubbles are more likely to nucleate on rough surfaces, such as a catalytic layer or channel defects. During the bubble growth, a gas depletion layer forms around the bubble, thus increasing the gas flux from the bulk liquid towards the bubble [28]. In addition, the presence of temperature gradients at the bubble-liquid interface can lead to variations in the surface tension at this interface, which may in turn result in additional surface flows, also known as the Marangoni effect [29].

Furthermore, the geometry and contact area of the bubble on the catalytic surface depend on the surface properties of the catalyst. In this study, bubbles with a protrusion angle α up to 90° were considered. However, bubbles can adopt more spherical shapes, have much smaller contact areas with the catalyst, and therefore do not cover the catalytic surface as much as hypothesized in this work. Furthermore, spherical bubbles also possibly give rise to corner flows, which would enhance mixing. Altogether, spherical bubbles are expected to limit the conversion to a lesser extent than bubbles considered in this study, which will be the topic of further research.

4 Conclusion

Transport phenomena in multiphase catalytic microreactors, where bubbles grow on a catalytic surface, are relatively complex. Here, the momentum, heat and mass transfer in a multiphase microreactor were studied using a 2D COMSOL simulation for different bubble mattress characteristics (length, protrusion angle, and catalytic surface coverage), and APR as a model reaction. As expected, the presence of bubbles decreased the overall chemical conversion, as they partially blocked the catalytic surface: the larger the bubbles, the lower the conversion. Although bubbles have a no-shear surface, the existence of a slip velocity was not sufficient to compensate for the loss of catalytic surface. For the considered endothermic APR reaction, the temperature in the fluidic channel was reduced, which in turn affected the diffusivity of the reactants to the catalytic surface. Altogether, this work highlights the importance of understanding the effect of bubbles on the interconnected transport phenomena in microreactors.

Acknowledgment

This work was supported by the Netherlands Center for Multiscale Catalytic Energy Conversion (MCEC), an NWO Gravitation program funded by the Ministry of Education, Culture and Science of the government of the Netherlands.

The authors have declared no conflict of interest.

Symbols used

b	[m]	slip length
c_i	[mol]	concentration species i
C_p	[J kg^{-1}K^{-1}]	heat capacity
D_i	[m^{2}s^{-1}]	diffusion constant species i
f_g	[N m^{-3}]	volume force due to gravity
k	[W m^{-1}K^{-1}]	thermal conductivity
L_g	[m]	characteristic bubble length
P	[bar]	pressure
q	[W m^{-2}]	heat flux
Re	[–]	Reynolds number
T	[K]	temperature
T_H	[K]	heater temperature
u	[m s^{-1}]	mean velocity

Greek letters

δ	[m]	thickness of the gas layer
μ_i	[Pa s]	viscosity
α	[°]	protrusion angle
ε_B	[–]	catalytic surface coverage
ρ	[kg m^{-3}]	density

Subscripts

g	gas
Gly	glycerol
l	liquid

Abbreviation

APR	aqueous-phase reforming

References

[1] R. D. Cortright, R. R. Davda, J. A. Dumesic, *Nature* **2002**, *418 (6901)*, 964–967. DOI: https://doi.org/10.1038/nature01009

[2] M. Worner, *Microfluidics Nanofluidics* **2012**, *12 (6)*, 841–886. DOI: https://doi.org/10.1007/s10404-012-0940-8
[3] J. Gomez-Pastora, C. Gonzalez-Fernandez, M. Fallanza, E. Bringas, I. Ortiz, *Chem. Eng. J.* **2018**, *344*, 487–497. DOI: https://doi.org/10.1016/j.cej.2018.03.110
[4] J. Stafford, *Int. J. Heat Mass Transfer* **2016**, *100*, 508–521. DOI: https://doi.org/10.1016/j.ijheatmasstransfer.2016.04.037
[5] J. Jimenez-Martinez, M. L. Porter, J. D. Hyman, J. W. Carey, H. S. Viswanathan, *Geophys. Res. Lett.* **2016**, *43 (1)*, 196–205. DOI: https://doi.org/10.1002/2015gl066787
[6] B.-B. Xu, Y.-L. Zhang, S. Wei, H. Ding, H.-B. Sun, *ChemCatChem* **2013**, *5 (8)*, 2091–2099. DOI: https://doi.org/10.1002/cctc.201200863
[7] R. Munirathinam, J. Huskens, W. Verboom, *Adv. Synth. Catal.* **2015**, *357 (6)*, 1093–1123. DOI: https://doi.org/10.1002/adsc.201401081
[8] R. Porta, M. Benaglia, A. Puglisi, *Org. Process Res. Dev.* **2016**, *20 (1)*, 2–25. DOI: https://doi.org/10.1021/acs.oprd.5b00325
[9] I. Iliuta, M. Hamidipour, D. Schweich, F. Larachi, *Chem. Eng. Sci.* **2012**, *73*, 299–313. DOI: https://doi.org/10.1016/j.ces.2012.02.007
[10] W. He, Z. Fang, K. Zhang, T. Tu, N. Lv, C. Qiu, K. Guo, *Chem. Eng. J.* **2018**, *331*, 161–168. DOI: https://doi.org/10.1016/j.cej.2017.08.103
[11] L. Zhu, C. Fu Tan, M. Gao, G. W. Ho, *Adv. Mater.* **2015**, *27 (47)*, 7713–7719. DOI: https://doi.org/10.1002/adma.201503828
[12] G. Chen, X. Zhu, R. Chen, Q. Liao, D. Ye, H. Feng, J. Liu, M. Liu, *Chem. Eng. J.* **2018**, *334*, 1897–1904. DOI: https://doi.org/10.1016/j.cej.2017.11.126
[13] A. Tanimu, S. Jaenicke, K. Alhooshani, *Chem. Eng. J.* **2017**, *327*, 792–821. DOI: https://doi.org/10.1016/j.cej.2017.06.161
[14] M. F. N. D'Angelo, V. Ordomsky, V. Paunovic, J. van der Schaaf, J. C. Schouten, T. A. Nijhuis, *ChemSusChem* **2013**, *6 (9)*, 1708–1716. DOI: https://doi.org/10.1002/cssc.201200974
[15] J. Ou, B. Perot, J. P. Rothstein, *Phys. Fluids* **2004**, *16 (12)*, 4635–4643. DOI: https://doi.org/10.1063/1.1812011
[16] L. Bocquet, J. L. Barrat, *Soft Matter* **2007**, *3 (6)*, 685–693. DOI: https://doi.org/10.1039/b616490k
[17] O. I. Vinogradova, A. L. Dubov, *Mendeleev Commun.* **2012**, *22 (5)*, 229–236. DOI: https://doi.org/10.1016/j.mencom.2012.09.001
[18] J. Ou, J. P. Rothstein, *Phys. Fluids* **2005**, *17 (10)*, 103606. DOI: https://doi.org/10.1063/1.2109867
[19] L. Bocquet, E. Lauga, *Nat. Mater.* **2011**, *10*, 334. DOI: https://doi.org/10.1038/nmat2994
[20] E. Karatay, P. A. Tsai, R. G. H. Lammertink, *Soft Matter* **2013**, *9 (46)*, 11098–11106. DOI: https://doi.org/10.1039/c3sm51928g
[21] AB COMSOL, *COMSOL Multiphysics 5.3a*, Stockholm **2018**.
[22] R. M. Ripken, S. Schlautmann, R. G. P. Sanders, J. G. E. Gardeniers, S. Le Gac, *Electrophoresis* **2019**, *40 (4)*, 563–570. DOI: https://doi.org/10.1002/elps.201800431
[23] R. R. Davda, J. W. Shabaker, G. W. Huber, R. D. Cortright, J. A. Dumesic, *Appl. Catal., B* **2005**, *56 (1–2)*, 171–186. DOI: https://doi.org/10.1016/j.apcatb.2004.04.027
[24] https://www.engineeringtoolbox.com/convective-heat-transfer-d_430.html (Accessed June, 2018)
[25] https://www.engineersedge.com/heat_transfer/convective_heat_transfer_coefficients__13378.html (Accessed June, 2018)
[26] S. Adhikari, S. D. Fernando, A. Haryanto, *Chem. Eng. Technol.* **2009**, *32 (4)*, 541–547. DOI: https://doi.org/10.1002/ceat.200800462
[27] J. R. Rumble, 99th ed., *Handbook of Chemistry and Physics*, CRC Press, Boca Raton, FL **2018**.
[28] P. Lv, H. Le The, J. Eijkel, A. Van den Berg, X. H. Zhang, D. Lohse, *J. Phys. Chem. C* **2017**, *121 (38)*, 20769–20776. DOI: https://doi.org/10.1021/acs.jpcc.7b04994
[29] A. Faghri, Y. Zhang, in *Transport Phenomena in Multiphase Systems* (Eds: A. Faghri, Y. Zhang), Academic Press, Boston **2006**, 331–420.

